



Consideration of microstructural effects in the analysis of adiabatic shear bands in a tungsten heavy alloy

R.C. Batra *, B.M. Love

Department of Engineering Science and Mechanics, MIC 0219, Virginia Polytechnic Institute and State University, Blacksburg, VA 24061, United States

Received 23 October 2005; received in final revised form 3 January 2006
Available online 9 March 2006

Abstract

We use multiscale and multiphysics analyses to approximately account for the microstructure of a composite comprised of tungsten particulates embedded in a nickel–iron matrix and deformed in plane strain tension at a high strain rate. Both materials are assumed to be perfectly bonded to each other, and heat-conducting, microporous, strain- and strain-rate hardening, and thermally softening with thermomechanical material parameters degrading with the evolution of porosity. The square region whose finite thermomechanical deformations are analyzed is divided into a uniform mesh, (for example), of 10×10 super-elements or patches, and each patch is subdivided into 10×10 uniform finite elements (FEs). Material properties in a super-element are obtained from those of its constituents and their volume fractions by a homogenization technique. Thus the square region is comprised of 100 homogeneous subbodies perfectly bonded to each other. Keeping the total number of FEs fixed, the effect of the number of patches on the time of initiation of an adiabatic shear band (ASB) is delineated, and it is compared with that obtained from the mesoscale analysis of the problem with the 100×100 uniform FE mesh and considering each material separately. With an increase in the number of patches, the ASB initiation time converges to that obtained from the mesoscale analysis. The CPU time and other computational resources required for the patchwork analysis are considerably less than those needed for the mesoscale analysis. The proposed technique enables one to consider effects of microstructure in analyzing deformations of a full-scale structure.

© 2006 Elsevier Ltd. All rights reserved.

* Corresponding author. Tel.: +1 540 231 6051; fax: +1 540 231 4574.
E-mail addresses: rbatra@vt.edu (R.C. Batra), brlove@vt.edu (B.M. Love).

Keywords: Multiscale and multiphysics analysis; Microstructural considerations; Adiabatic shear bands; Thermoelastoviscoplasticity; Large deformations; Finite element method

1. Introduction

An adiabatic shear band (ASB) is a narrow region, usually a few micrometers (microns) wide, of intense plastic deformation that generally forms in metals deformed at high strain rates. Their study is important since they invariably precede ductile fracture. Tresca (1878) observed them during the hot forging of a platinum bar and called them “hot lines”. Even though heat conduction plays a significant role in determining their widths and spacing between adjacent shear bands, they are called adiabatic since there is not enough time for the heat produced due to plastic working to be conducted out of them. Batra and Kim (1991) have shown, through numerical experiments, that the consideration of heat conduction has negligible effect on the ASB initiation time but influences the band width; however, for high heat conducting materials such as copper and/or when thermal loads are significant (Batra and Wei, 2006), heat conduction must be considered. Most experimental, analytical and numerical works on ASBs have assumed the material to be homogeneous and isotropic (e.g., see Batra (1987, 1988); Batra and Kim (1990a,b, 1991); Batra and Ko (1992, 1993); Wright (2002); Bai and Dodd (1992)); exceptions to this include the experimental studies of Dick et al. (1991), Wei et al.’s (2001), and Dai et al. (2004), one-dimensional analytical/numerical analysis of Charalambakis and Baxevanis (2004), and two-dimensional numerical studies of Batra and Love (2004, 2005a,b), and of Chatzigeorgiou and Charalambakis (2005). For a homogeneous material, Batra and Kim (1992) and Batra and Lear (2005) have adopted the following ASB initiation criterion: an ASB initiates at a point when the maximum shear stress there has dropped to 80% of its peak value at that material point, and it is deforming plastically. Batra and Love (2005b) have reported that this criterion fails for particulate composites even though it can be successfully used for functionally graded materials in which material properties vary continuously within the body (e.g., see Batra and Love, 2004). For a tungsten (W)/nickel–iron (NiFe) particulate composite, they found that this criterion was satisfied at a material point at time t_1 but failed there at a subsequent time t_2 . Until the time a coherent ASB had formed, material points where this criterion had been met did not necessarily lie on a contiguous curve or within a simply connected region. Furthermore, contours of the effective plastic strain used here to fore to identify ASBs (e.g., see Needleman (1989); Batra and Liu (1989); Zhu and Batra (1990)), could not be used to delineate an ASB. Batra and Love (2005b) have proposed that an ASB initiates at a material point, when the rate of increase of the specific energy dissipation rate there increases by an order of magnitude. We adopt this criterion to analyze the initiation of ASBs in a W/NiFe particulate composite by two methods – a mesoscale analysis in which material properties of each constituent are considered, and a multiscale analysis which divides the cross-section into a suitable number of patches, and material in each patch is assumed to be homogeneous with properties derived from those of its constituents and their volume fractions.

We note that the characteristic time and the characteristic length for the thermal and the mechanical problems are quite different. Here nonlinear coupled thermomechanical deformations of the particulate composite have been analyzed. Energy dissipated due to plastic deformations influences the heat produced, and hence the temperature rise of a

particulate which in turn softens it and causes it to deform more severely and rapidly. The multiphysics analysis refers to solving the two-way coupled transient thermomechanical problem.

The assumption of plane strain deformations implies that W particulates are cylinders with axes perpendicular to the plane of deformation; here these are assumed to be randomly distributed uniform circular cylinders. However, one actual microstructure from Wei et al.'s (2001) paper that describes experimental work on dynamic deformations of tungsten heavy alloy (WHA) rods has also been studied.

Previously, Batra and Love (2006a) used the following multiscale approach to analyze ASBs in a WHA. The $10\text{ mm} \times 10\text{ mm}$ region was divided into a uniform mesh of 200×200 elements and assumed to be made of a homogeneous and isotropic material whose properties were deduced from those of its isotropic constituents and their volume fractions by the rule of mixtures. Coupled thermomechanical deformations were assumed to be symmetric about the horizontal and the vertical centroidal axes. Plane strain deformations of the $5\text{ mm} \times 5\text{ mm}$ region in the first quadrant were analyzed, and time histories of velocities, temperature and stresses at nodes on the boundaries of the $1\text{ mm} \times 1\text{ mm}$ subregion with the bottom left corner coincident with the corresponding vertex of the $5\text{ mm} \times 5\text{ mm}$ region were recorded. Subsequently, the actual microstructure in the $0.5\text{ mm} \times 0.5\text{ mm}$ subregion of the $1\text{ mm} \times 1\text{ mm}$ region was considered with the remaining region comprised of the homogenized material used in the earlier analysis; bottom left corners of the $0.5\text{ mm} \times 0.5\text{ mm}$ and the $1\text{ mm} \times 1\text{ mm}$ regions coincided with each other. When time histories of velocity and temperature were prescribed on the boundaries of the $1\text{ mm} \times 1\text{ mm}$ region, the analysis failed in the sense that the solution did not converge. However, the analysis ran smoothly with time histories of tractions and temperature assigned on these boundaries. The ASB initiation time computed from this multiscale analysis equaled $22\text{ }\mu\text{s}$ whereas that found from the mesoscale analysis of the $5\text{ mm} \times 5\text{ mm}$ region was $58\text{ }\mu\text{s}$. However, the ASB initiation time predicted from the present patchwork approach is very close to that obtained from the mesoscale analysis, and the difference between the two can be minimized by systematically increasing the number of patches.

The rest of the paper is organized as follows. Section 2 gives formulation of the problem that includes governing equations, constitutive relations, and initial and boundary conditions, the Galerkin approximation of the problem, and a description of the technique to determine values of thermomechanical parameters of the homogenized body equivalent to the given particulate composite. Section 3 describes the multiscale analysis approach, and compares results computed using this method with those obtained from the mesoscale analysis. Results from a hypothetical microstructure, and an actual microstructure with 90% volume fraction of W, taken from Wei et al.'s (2001) paper, are presented in Section 3. Conclusions drawn from this work are summarized in Section 4.

2. Formulation of the problem

Fig. 1a depicts the microstructure of a $2\text{ mm} \times 2\text{ mm}$ sample of a WHA containing 50% volume fraction of $50\text{ }\mu\text{m}$ diameter W particulates, shown dark, randomly distributed in NiFe matrix, depicted light grey; the microstructure of a WHA with 90% volume fraction of W is exhibited in Fig. 4a. The sample of Fig. 1a is divided into 10×10 uniform super-elements. Within each super-element material properties are assumed to be homogeneous,

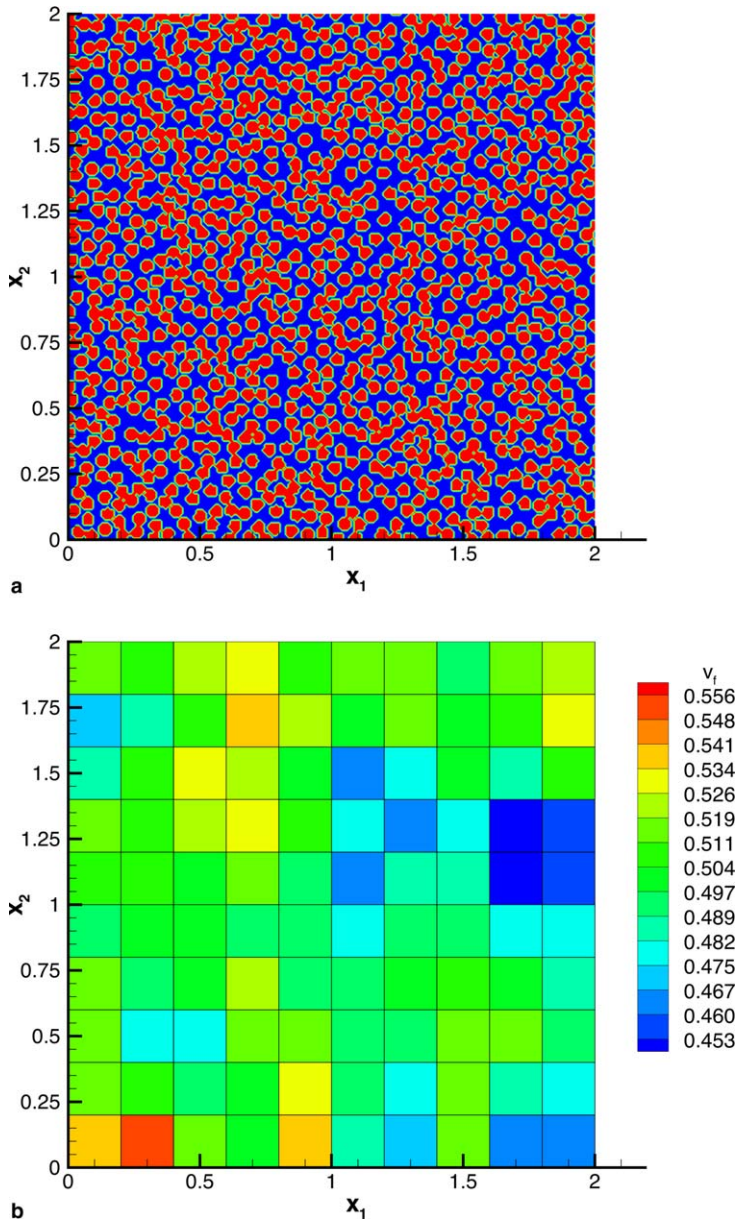


Fig. 1. (a) 2 mm \times 2 mm particulate composite consisting of 50% volume fraction of 50 μm diameter W particulates randomly embedded in a NiFe matrix. (b) Inhomogeneous body generated when the body in (a) is divided into 10×10 uniform and homogeneous super-elements.

and derived from those of its constituents and their volume fractions as described in Section 2.3; the inhomogeneous body so obtained is exhibited in Fig. 1b. The volume fraction of W in these super-elements varies from 45.3% to 55.6%. Thus, the sample is divided into uniform 100 inhomogeneous bodies. Whereas the microstructure of Fig. 1a is generated

with a computational algorithm, a microstructure used in experiments and containing 90% volume fraction of W has also been analyzed in Section 3.

We assume that the particulate and the matrix materials can be modeled as isotropic, microporous and thermo-elasto-viscoplastic. We use rectangular Cartesian coordinates and the referential description of motion to describe their finite plane strain transient coupled thermomechanical deformations. Deformations of each constituent, and of the composite body are governed by Eqs. (1)–(4) expressing, respectively, the balance of mass, the balance of linear momentum, the balance of moment of momentum, and the balance of internal energy

$$\rho(1 - f)J = \rho_0(1 - f_0), \tag{1}$$

$$\rho_0(1 - f_0)\dot{v}_i = T_{ix,\alpha} + \rho_0 b_i, \quad i = 1, 2, \quad \alpha = 1, 2, \tag{2}$$

$$T_{ix}F_{j\alpha} = T_{j\alpha}F_{ix}, \tag{3}$$

$$\rho_0(1 - f_0)\dot{e} = -Q_{\alpha,\alpha} + T_{ix}\dot{F}_{ix} + \rho_0 s. \tag{4}$$

Here ρ is the present mass density, ρ_0 the mass density in the reference configuration, f the porosity (i.e., the volume fraction of voids at time t), f_0 the porosity in the reference configuration, $J = \det \mathbf{F}$, $F_{ix} = x_{i,\alpha} = \partial x_i / \partial X_\alpha$ the deformation gradient, \mathbf{x} the present position at time t of a material particle located at the place \mathbf{X} in the reference configuration, \mathbf{T} the first Piola–Kirchhoff stress tensor, e the specific internal energy, \mathbf{Q} the present heat flux measured per unit reference area, \mathbf{v} the velocity of a material particle, a superimposed dot indicates the material time derivative, a repeated index implies summation over the range of the index, \mathbf{b} the body force per unit mass, and s the specific source of internal energy. Typically, in solid mechanics, \mathbf{b} and s are taken as zeros. Greek indices refer to coordinates in the reference configuration, and Latin indices to coordinates in the present configuration. The porosity f is assumed to be uniformly distributed in each constituent, and can be regarded as a measure of the damage.

We assume that the strain-rate tensor \mathbf{D} defined by $D_{ij} = (v_{i,j} + v_{j,i})/2$, $v_{i,j} = \partial v_i / \partial x_j$, has the additive decomposition into an elastic part \mathbf{D}^e , a plastic part \mathbf{D}^p , and a thermal part $\hat{\alpha}\theta\mathbf{1}$, viz., $\mathbf{D} = \mathbf{D}^e + \mathbf{D}^p + \hat{\alpha}\theta\mathbf{1}$. Here $\hat{\alpha}$ is the coefficient of thermal expansion, θ the temperature rise, and $\mathbf{1}$ the identity tensor. Eqs. (1)–(4) are supplemented with the following constitutive relations.

$$\dot{\sigma}_{ij} + \sigma_{ik}W_{kj} + \sigma_{jk}W_{ki} = \frac{E(1 - f)}{1 + \nu}D_{ij}^e + \frac{E(1 - f)\nu}{(1 + \nu)(1 - 2\nu)}D_{kk}^e\delta_{ij}, \tag{5}$$

$$\dot{e} = cT\dot{\theta} + c\dot{\theta} + \frac{1}{\rho(1 - f)}\sigma_{ij}D_{ij}^e, \quad T_{ix} = J\sigma_{ij}(F^{-1})_{\alpha j}, \tag{6}$$

$$q_i = -\kappa\left(1 - \frac{3}{2}f\right)\theta_{,i}, \quad Q_\alpha = Jq_i(F^{-1})_{\alpha i}, \tag{7}$$

$$\phi \equiv \frac{\sigma_e^2}{\sigma_y^2} - 1 + 2f^*\beta_1 \cosh\left(\frac{3\beta_2\bar{p}}{2\sigma_y}\right) - \beta_1^2(f^*)^2 = 0, \quad \sigma_e^2 = \frac{3}{2}\sigma'_{ij}\sigma'_{ij}, \quad i, j = 1, 2, 3, \tag{8}$$

$$D_{ij}^p = \lambda \frac{\partial \phi}{\partial \sigma_{ij}} = \lambda \left[\frac{3\sigma'_{ij}}{\sigma_y^2} - \frac{f^*\beta_1\beta_2}{\sigma_y} \sinh\left(\frac{3\beta_2\bar{p}}{2\sigma_y}\right)\delta_{ij} \right], \quad \sigma'_{ij} = \sigma_{ij} + p\delta_{ij}, \tag{9}$$

$$p = -(\sigma_{11} + \sigma_{22} + \sigma_{33})/3, \quad \bar{p} = pH(-p - 0), \tag{10}$$

$$\dot{\lambda} = \begin{cases} \frac{(1-f)\sigma_y \dot{\epsilon}_e^p}{\sigma_{ij} \dot{\epsilon}_{ij}^p} & \text{if } \phi = 0 \quad \text{and} \quad \dot{\phi} \geq 0, \\ 0 & \text{when either } \phi < 0 \quad \text{or} \quad \phi = 0 \quad \text{and} \quad \dot{\phi} < 0, \end{cases} \tag{11}$$

$$\dot{f} = (1-f)D_{ii}^p + \frac{f_2 \dot{\epsilon}_e^p}{s_2 \sqrt{2\pi}} e^{-\frac{1}{2} \left(\frac{\epsilon_e^p - \epsilon_n}{s_2} \right)^2} H(-p-0), \tag{12}$$

$$f^* = \begin{cases} f, & f \leq f_c, \\ f_c + \frac{f_u - f_c}{f_f - f_c} (f - f_c), & f > f_c, \end{cases} \tag{13}$$

$$\sigma_y = (A + B(\epsilon_e^p)^n) \left(1 + \tilde{C} \ln \left(\frac{\dot{\epsilon}_e^p}{\dot{\epsilon}_0^p} \right) \right) \left(1 - \left(\frac{\theta - \theta_r}{\theta_m - \theta_r} \right)^m \right). \tag{14}$$

The left-hand side of Eq. (5) equals the Jaumann derivative of the Cauchy stress tensor σ , $W_{ij} = (v_{i,j} - v_{j,i})/2$ is the spin tensor, E Young’s modulus, and ν Poisson’s ratio. Constitutive relation (5) implies that each constituent is being modeled as an isotropic hypoelastic material. Replacing the Jaumann derivative of σ by another objective stress rate will change the constitutive description of the material. However, Batra and Jaber (2001) found that it does not alter the ASB initiation time in a homogeneous thermoviscoplastic material mainly because elastic deformations are negligible as compared to the plastic deformations within an ASB and in regions adjacent to it. Similarly, adopting another constitutive relation, such as that for a hyperelastic material, will not affect the ASB initiation time. Eq. (6)₁ is the constitutive relation for the internal energy, e . In it c is the specific heat, and τ the thermal relaxation time that equals the time required to establish a steady state of heat conduction in an element suddenly exposed to heat flux. Fourier’s law of heat conduction is described by Eq. (7)₁ in which κ is the thermal conductivity of the solid material, and θ the present temperature of a material particle. Eq. (6)₂ relates \mathbf{T} and σ .

In the yield surface (8) proposed by Gurson (1977) for a porous material, p is the hydrostatic pressure given by Eq. (10)₁, and f^* the modified value of porosity given by (13). Gurson’s yield surface is based on quasistatic analysis with the matrix material modeled as rigid perfectly plastic and obeying von Mises yield criterion. Constants β_1 and β_2 , introduced by Tvergaard and Needleman (1984), provide a better fit of results computed from a FE analysis of the formation of ASBs in a plate having an array of large cylindrical voids with test observations. Eq. (9)₁ is the associative flow rule requiring that the current value of the plastic strain rate be along the normal to the yield surface with $\dot{\lambda}$, the factor of proportionality, defined by (11); $\dot{\lambda} > 0$ only when the material point is deforming plastically.

Eq. (12) gives the evolution of porosity; the first term on its right-hand side is derived by assuming that the matrix is incompressible and the elastic dilatation is negligible as compared to the plastic dilatation, and the second term is the strain based nucleation of voids introduced by Chu and Needleman (1980). f_2 , s_2 and ϵ_n are material parameters; the rate of nucleation of voids is highest when ϵ_e^p equals ϵ_n and decays exponentially with the difference between ϵ_e^p and ϵ_n . H is the Heaviside step function. We have thus assumed that new voids nucleate only when the hydrostatic stress is tensile. To account for the coalescence of neighboring voids, Tvergaard and Needleman (1984) enhanced the porosity, as given by Eq. (13), after it reaches its critical value f_c . In Eq. (13), f_f is the porosity at ductile fracture, and $f_u = 1/\beta_1$ is the porosity when the yield surface has shrunk to a point. Wei and Batra (2002) have proposed that $\dot{f} = 0.566 (\exp[\sigma_{kk}/2\sigma_y]) \dot{\epsilon}_e^p H(-p-0)$.

In the Johnson and Cook (1983) relation (14) σ_y , the current yield stress of the material, depends upon the effective plastic strain ε_p^p , the effective plastic strain rate $\dot{\varepsilon}_p^p$, and the temperature θ . Furthermore A , B , \tilde{C} , $\dot{\varepsilon}_0^p$, and m are material parameters, θ_r the room temperature, and θ_m the fictitious melting temperature of the material in the sense that it is a curve fitting parameter rather than the actual melting temperature. Parameters B and n characterize the strain hardening of the material, \tilde{C} and $\dot{\varepsilon}_0^p$ the strain-rate hardening, and the last factor on the right-hand side of Eq. (14) its thermal softening.

Eqs. (8) and (14) imply that the radius of the von Mises yield surface increases due to strain- and strain-rate hardening of the material but decreases due to the softening induced by the temperature rise and the increase in porosity. The degradation of material properties due to the damage, taken here synonymous with the porosity, is indicated by Eqs. (5)–(8). The affine variation with the porosity of Young's modulus, the bulk modulus, the stress-temperature coefficient, and the heat capacity implies that the rule of mixtures has been employed to find their effective values; the expression for the thermal conductivity in Eq. (7)₁ is due to Budiansky (1990). The interaction, if any, among neighboring voids has been tacitly ignored. Jiang and Batra (2002), among others, have considered this interaction. The shrinkage of the yield surface due to an increase in porosity described by Eq. (8) can be seen by plotting the yield surface for two different values of f while keeping other variables fixed.

Depending upon the values of material parameters, softening induced by the increase in porosity can exceed that due to temperature rise and induce the initiation of an ASB; e.g., see Batra and Jin (1994).

We have described damage by porosity rather than by the Johnson–Cook type relation since the dependence of the yield surface and other material parameters upon the latter is unknown. Neither the porosity evolution nor the time history of the Johnson–Cook damage variable can be measured experimentally in metals undergoing high strain rate deformations.

We note that the problem formulation incorporates thermal stresses developed due to the differences in the coefficients of thermal expansion of the constituents.

For plane strain deformations, $D_{33} = D_{13} = D_{23} = D_{13}^\theta = D_{23}^\theta = D_{13}^p = D_{23}^p = 0$ but D_{33}^p and D_{33}^θ are, in general, nonzero.

For metallic alloys the parabolic and the hyperbolic heat equations give essentially the same ASB initiation time. As stated earlier in Section 1, if the objective is to find the ASB initiation time, one can neglect heat conduction, except possibly for copper. However, the spacing between adjacent ASBs, and the width of an ASB are affected by the value of thermal conductivity.

Substitution for $\dot{\varepsilon}$ and q_i from Eq. (6)₁ and (7) into Eq. (4) gives the following hyperbolic heat equation:

$$\rho_0(1 - f_0)c(\tau\ddot{\theta} + \dot{\theta}) = \left(\kappa \left(1 - \frac{3}{2}f \right) \theta_{,x} \right)_{,x} + J\sigma_{ij}D_{ij}^p + \rho_0s. \quad (15)$$

The term $J\sigma_{ij}D_{ij}^p$ equals the heating due to plastic working per unit volume in the reference configuration; thus the Taylor–Quinney parameter has been taken as 1. Except for a delay in the time of initiation of an ASB other results remain unaffected by a lower value of the Taylor–Quinney factor. The form (15) of the hyperbolic heat equation is due to Cattaneo (1958) and Vernotte (1958). Batra and Lear (2005), and Batra and Chen (1999) found that the finiteness of the thermal wave speed affects the ASB initiation time in a typical steel, and the spacing between adjacent shear bands only when $\tau \geq 10^{-6}$ s.

For a typical steel, $\tau = 1 \times 10^{-12}$ s, and $\tau \approx 25 \times 10^{-12}$ s for copper. For these values of τ Batra and Lear (2005) found that the hyperbolic and the parabolic heat equations give identical values of the ASB initiation time. Batra (1975) considered higher-order spatial and temporal gradients of temperature, and derived a heat equation that admits finite speeds of thermal waves. However, in such a material either a thermal wave propagates with a finite speed or the linearized problem has a unique solution. Ideally, one will like to have both.

We note that Batra and Kim (1990), Batra and Jaber (2001), and Batra and Chen (1999) have analyzed different aspects of shear banding with four different thermoviscoplastic relations, namely, the Johnson and Cook (1983), the Litonski–Batra (e.g., see Batra (1988)), the Bodner and Partom (1975) and a power law. These relations were calibrated to give nearly the same effective stress vs. the effective strain curve during homogeneous deformations of the body. However, during inhomogeneous deformations, each one of the relations gave qualitatively similar but quantitatively different results. The decision to use the Johnson–Cook relation here is based on the availability of values of thermomechanical parameters for W and NiFe.

2.1. Initial and boundary conditions

The body is initially at rest, stress free, at a uniform temperature, has zero rate of change of temperature, and a prescribed initial porosity. Thus

$$\begin{aligned} \mathbf{x}(\mathbf{X}, 0) = \mathbf{X}, \quad \mathbf{v}(\mathbf{X}, 0) = \mathbf{0}, \quad \theta(\mathbf{X}, 0) = \theta_0, \quad \dot{\theta}(\mathbf{X}, 0) = 0, \quad \rho(\mathbf{X}, 0) = \rho_0(\mathbf{X}), \\ \boldsymbol{\sigma}(\mathbf{X}, 0) = \mathbf{0}, \quad \varepsilon_e^p(\mathbf{X}, 0) = 0, \quad f(\mathbf{X}, 0) = f_0(\mathbf{X}), \quad \mathbf{X} \in \Omega. \end{aligned} \quad (16)$$

Here Ω is the region occupied by the body in the reference configuration.

We assume that the body is prismatic having a uniform cross-section, and the volume fractions of constituents, initial conditions, and boundary conditions are independent of the axial coordinate. We thus assume that a plane strain state of deformation prevails in the body. Furthermore, for the body deformed in simple tension, the initial cross-section is square of side $2H$, and thermomechanical deformations are assumed to be symmetric about the two centroidal axes. Thus the compositional profile has been tacitly assumed to be symmetric about the two centroidal axes.

Tensile deformations of one-quarter of the cross-section, shown in Fig. 1a, are analyzed. Boundary conditions (17)_{4–6} and (17)_{7–9}, listed below, arising from the symmetry of deformations are imposed at points on the centroidal axes $X_1 = 0$ and $X_2 = 0$. The vertical surface $X_1 = H$ is taken to be traction free and thermally insulated; see Eq. (17)_{1–3}. Normal velocity, null tangential tractions, and zero heat flux are prescribed on the top horizontal surface $X_2 = H$; these are given by Eq. (17)_{10–12}. The prescribed normal velocity, given by Eq. (17)₁₂, increases linearly with time to its steady state value v_0 in $1 \mu\text{s}$ and is then held fixed.

$$\begin{aligned} T_{21} = T_{11} = 0, \quad Q_1 = 0 \quad \text{on } X_1 = H, \\ T_{21} = 0, \quad v_1 = 0, \quad Q_1 = 0 \quad \text{on } X_1 = 0, \\ T_{12} = 0, \quad v_2 = 0, \quad Q_2 = 0 \quad \text{on } X_2 = 0, \\ T_{12} = 0, \quad Q_2 = 0, \quad v_2 = \begin{cases} v_0(t/1 \mu\text{s}), & 0 \leq t \leq 1 \mu\text{s}, \\ v_0, & t \geq 1 \mu\text{s}, \end{cases} \quad \text{on } X_2 = H. \end{aligned} \quad (17)$$

2.2. Interface conditions

It is assumed that, during the entire deformation process, the W particulates are both mechanically and thermally perfectly bonded to the NiFe matrix. Thus

$$[\mathbf{u}] = \mathbf{0}, \quad [\theta] = 0, \quad [T_{i\alpha}N_\alpha] = 0, \quad [Q_\alpha N_\alpha] = 0 \quad \text{on } \Gamma, \quad (18)$$

where \mathbf{N} is an outward unit normal, in the reference configuration, to the interface Γ between a particulate and the matrix, and the square bracket indicates the jump of a quantity across the interface Γ between a particulate and the matrix. This assumption is reasonable since a WHA is usually manufactured by sintering in which the composite material is heated to a temperature close to the melting temperature of the matrix and subjected to a high pressure.

2.3. Material properties for the equivalent homogenized body

There are no micromechanics based relations available to compute values of all material parameters of a composite comprised of thermo-elasto-viscoplastic constituents. Values of E , ν , κ , α , ρ and c for the equivalent homogenized medium can be computed by using a micromechanics based model such as that proposed by Mori and Tanaka (1973), but those of A , B , \tilde{C} , m , n and θ_m cannot be so found. We note that the melting temperature θ_m for the composite will equal the lowest temperature at which one of its constituents melts. The value of θ_m for the equivalent homogenized medium equals a fictitious number obtained by fitting the Johnson–Cook relation (14) to the data from either physical or numerical experiments. Numerical plane strain tension tests on representative volume elements (RVEs) of different sizes containing varying volume fractions of random and/or ordered arrangements of particulates of circular cross-section were performed; e.g., see Batra and Love (2006b). Values of E , κ , α , B , \tilde{C} , n and θ_m obtained from these numerical experiments were found to differ by at most 10% from their values computed by the rule of mixtures. According to this rule, the value P of a material parameter for a mixture comprised of two constituents with volume fractions V_1^f and V_2^f and values P_1 and P_2 of the material parameter is given by

$$P = V_1^f P_1 + V_2^f P_2 = (1 - V_2^f) P_1 + V_2^f P_2. \quad (19)$$

It gives exact values of the mass density and the heat capacity, and is simple to use. It ignores interactions among adjacent particulates, their shapes, sizes and orientations, and their distribution in the matrix. Here the rule of mixtures, Eq. (19), has been used to ascertain values of material parameters of the W/NiFe composite.

2.4. Semi-discrete formulation of the problem

Eqs. (5), (6)₂ and (3) imply that the balance of moment of momentum (3) is identically satisfied. The present mass density can be computed from Eq. (1) if the deformation gradient and the current value of the porosity are known. Thus, the dependent variables to be solved for are \mathbf{x} , f and θ and the independent variables are \mathbf{X} and t . Eqs. (2) and (15) are second-order coupled non-linear hyperbolic partial differential equations for \mathbf{x} and θ . These can not be written explicitly in terms of \mathbf{x} and θ since \mathbf{T} is given by (6)₂ and $\dot{\sigma}$ by (5) which involves \mathbf{D}^p and θ . We solve the problem numerically by the finite element method (FEM).

We first introduce an auxiliary variable $\xi = \dot{\theta}$. Let $\psi_1, \psi_2, \dots, \psi_n$ be the FE basis functions defined on Ω . We write

$$v_i = \sum_{A=1}^{\text{nodes}} \psi_A(\mathbf{X}) \tilde{v}_{Ai}(t), \quad \theta = \sum_{A=1}^{\text{nodes}} \psi_A(\mathbf{X}) \tilde{\theta}_A(t), \quad \xi = \sum_{A=1}^{\text{nodes}} \psi_A(\mathbf{X}) \tilde{\xi}_A(t), \quad i = 1, 2. \quad (20)$$

Here $\tilde{\mathbf{v}}$ is the vector of velocities of nodes, $\tilde{\boldsymbol{\theta}}$ the vector of nodal temperatures, and $\tilde{\boldsymbol{\xi}}$ the vector of rate of change of temperature at the nodes. Following the usual procedure, e.g. see Hughes (1987), we get

$$\mathbf{M}\dot{\tilde{\mathbf{v}}} = \mathbf{F}^{\text{ext}} - \mathbf{F}^{\text{int}}, \quad \dot{\tilde{\boldsymbol{\theta}}} = \tilde{\boldsymbol{\xi}}, \quad \boldsymbol{\tau} \mathbf{H} \tilde{\boldsymbol{\xi}} = \mathbf{F}^\theta + \tilde{\mathbf{Q}}, \quad (21)$$

where

$$\begin{aligned} M_{AB} &= \int_{\Omega} \rho_0(1 - f_0) \psi_A \psi_B \, d\Omega, & F_{Ai}^{\text{int}} &= \int_{\Omega} \psi_{A,x} T_{ix} \, d\Omega, & F_{Ai}^{\text{ext}} &= \int_{\Omega} \psi_A \rho_0 b_i \, d\Omega, \\ H_{AB} &= \int_{\Omega} \rho_0 c(1 - f_0) \psi_A \psi_B \, d\Omega, & F_A^\theta &= \int_{\Omega} \kappa \left(1 - \frac{3}{2} f\right) \theta_{,x} \psi_{A,x} \, d\Omega, & & \\ Q_A &= \int_{\Omega} \psi_A (\rho_0 s + J \text{tr}(\boldsymbol{\sigma} \mathbf{D}^p)) \, d\Omega. & & & & \end{aligned} \quad (22)$$

Note that the natural boundary conditions of zero heat flux on all bounding surfaces, and null surface tractions on $X_1 = H$, zero tangential tractions on $X_2 = 0, H$, and $X_1 = 0$, have been embedded in Eq. (21). For non-zero surface tractions, and nonvanishing heat flux prescribed on a part of the boundary, Eq. (22)₂ and (22)₄ are suitably modified.

In the Lagrangian formulation of the problem, matrices \mathbf{M} and \mathbf{H} are computed only once but matrices \mathbf{F}^{int} , \mathbf{F}^θ and $\tilde{\mathbf{Q}}$ are computed after every time step. These matrices are modified to incorporate essential boundary conditions (17)₁₂.

We solve Eq. (14) for $\dot{\varepsilon}_e^p$ in terms of σ_y , ε_e^p and θ , and integrate the resulting equation along with Eqs. (5) and (12) at the integration (or Gauss quadrature) points. Recall that $\dot{\varepsilon}_e^p > 0$ only when a material point is deforming plastically as signified by the satisfaction of Eq. (8)₁; otherwise $\dot{\varepsilon}_e^p = 0$. Weak form of equation $\dot{\mathbf{x}} = \mathbf{v}(\mathbf{X}, t)$ is also derived. We thus get coupled nonlinear ordinary differential equations (ODEs)

$$\dot{\mathbf{d}} = \mathbf{F}, \quad (23)$$

where \mathbf{d} is the vector of unknowns, and \mathbf{F} is the force vector that depends upon time t and $\mathbf{d}(t)$. The six unknowns at a node are $\{x_1, x_2, v_1, v_2, \theta, \xi\}$, and the dimension of vector \mathbf{d} equals 6 times the number of nodes. Furthermore, unknowns at a quadrature point are $\{\sigma_{11}, \sigma_{22}, \sigma_{12}, \sigma_{33}, f, \varepsilon_e^p\}$. Thus the total number of coupled ODEs to be integrated equal 6 (number of nodes) + 6 × 4 × (number of elements) for a 2 × 2 integration rule. Batra and Jaber (2001) employed a similar technique to numerically solve the coupled thermoviscoplastic problem. They used a FE mesh comprised of triangular elements and one-point integration rule to compute the domain integrals.

3. Computation of results

A computer code employing 4-node isoparametric quadrilateral elements has been developed. Integrals in Eq. (22) over each element are evaluated by using the 2 × 2 Gauss quadrature rule. Should a FE span two materials, values of the material parameters at the

Gauss quadrature point are used. Batra (1980) used this procedure for analyzing finite static deformations of an inhomogeneous cylinder made of a Mooney–Rivlin material and showed that computed results matched well with the analytical solution. The coupled non-linear ODEs (23) are integrated with respect to time t by using the subroutine LSODE (Livermore Solver for ODEs) developed by Hindmarsh (1983). It adjusts adaptively the time step and the order of the integration scheme so as to compute a stable solution within the prescribed absolute and relative tolerances. Because of the large number of nodes in the FE mesh, the Adams–Moulton integration method obtained by setting $MF = 10$ in LSODE is employed. Variables RTOL and ATOL that specify the relative and the absolute tolerances in the computed solution are each set equal to 10^{-6} .

Both the mechanical and the thermal problems are hyperbolic. As mentioned in Section 3.1, the speed of the thermal wave is considerably smaller than that of the mechanical waves, the latter controls the size of the time step. Once deformations begin to localize the time step drops significantly. This drop in the time step occurs at a lower value of the nominal strain for a particulate composite than that for the homogenized body. This is because inhomogeneities in deformations introduced by numerous particulate/matrix interfaces induce high strains, not necessarily simultaneously, at several discrete points in the body. The deformation may begin to localize at any one of these sites, and it eventually localizes into a connected region. For a 100×100 uniform FE mesh the CPU time is ~ 120 h on a SGI single processor Altix machine.

3.1. Values of material parameters

Values of thermophysical parameters for the W and the NiFe are listed in Table 1. Values of material parameters in the Johnson–Cook relation (14) are obtained by fitting curves to data points computed from the relations given by Zhou (1993). Zhou mentioned that the NiFe matrix phase also contained some W. Values assigned to other parameters given below in (24) are the same for the two constituents and for the homogenized body; we note that these are not readily available in the literature for different materials.

$$\begin{aligned} \beta_1 = 1.5, \quad \beta_2 = 1.0, \quad f_2 = 0.04, \quad s_2 = 0.1, \quad \varepsilon_n = 0.5, \quad \tau = 10^{-8} \text{ s}, \\ \theta_r = 273 \text{ K}, \quad f_c = 0.15, \quad f_u = 2/3, \quad f_f = 0.25. \end{aligned} \quad (24)$$

Thus the acoustic impedances of W and NiFe equal 87.86×10^6 and 48.44×10^6 kg/(m² s), respectively, and differ by a factor of 1.8. The bar wave speeds in W and NiFe are 4552 and 5265 m/s, respectively, and differ by a factor of 0.86. Speeds of a thermal disturbance in W and NiFe equal 77.5 and 53.34 m/s, respectively.

Table 1
Values of material parameters

| Material | ρ (kg/m ³) | E (GPa) | ν | κ (W/(m K)) | c (J/(kg K)) | α (10 ⁻⁶ /K) |
|-----------|-----------------------------|-----------|-------------|-----------------------------|----------------|--------------------------------|
| Tungsten | 19,300 | 400 | 0.29 | 160 | 138 | 5.3 |
| NiFe | 9200 | 255 | 0.29 | 100 | 382 | 15 |
| A (MPa) | B (MPa) | n | \tilde{C} | $\dot{\varepsilon}_0$ (1/s) | θ_m (K) | m |
| 730 | 562 | 0.075 | 0.290 | 10^{-6} | 1723 | 1.0 |
| 150 | 546 | 0.208 | 0.0838 | 10^{-6} | 1225 | 1.0 |

Because of the random distribution of W particulates the fraction of the axial load supported by W and NiFe at a horizontal surface $x_2 = \text{constant}$ varies with time t . Once either one or both of these constituents begin to deform plastically, speeds of incremental elastic waves in them will depend upon values of the tangent moduli. There are four non-zero components of the Cauchy stress tensor, and of the elastic strain tensor giving several elastic moduli for each material that need not vanish simultaneously. Also waves are reflected and refracted from interfaces between W and NiFe particulates, as well as reflected from the bounding surfaces. These make the deformation highly heterogeneous, and provide numerous sites for the initiation of ASBs.

3.2. Verification of code

The method of fictitious body forces (also called the method of manufactured solutions) is used to verify that the code correctly solves the initial- boundary-value problem defined by Eqs. (1)–(18). In this method, analytical expressions for the displacement and the temperature fields are presumed, and body forces \mathbf{b} and the source s of internal energy in Eqs. (2) and (4) are computed so as to satisfy the balance of linear momentum and the balance of internal energy. Also, initial and boundary conditions are derived from the assumed displacement and temperature fields. These are input into the code and the numerical solution is found. A good agreement between the computed and the analytical solutions verifies the code. This method was also used by Batra and Liang (1997, e.g. see remarks following Eq. (30), of their paper).

For an ASB problem involving a homogeneous material, computed results were also found to agree very well with those obtained by Batra and Lear (2005) who employed a similar problem formulation but used 3-node triangular elements for a numerical solution of the problem.

The code was used to study wave propagation in an inhomogeneous elastic bar (Batra and Love, 2005a). The time histories of the computed wave speed, and of the axial stress at a point were found to agree well with the analytical solution of Chiu and Erdogan (1999).

3.3. Adiabatic shear band initiation criterion

For both homogeneous and functionally graded bodies in which material parameters vary continuously with the position the following ASB initiation criterion has been successfully used. An ASB initiates at a point where the maximum shear stress has dropped to 80% of its peak value at that point, and the material point is still deforming plastically; e.g. see Batra and Lear (2005) and Batra and Love (2004). However, for high strain-rate deformations of a particulate composite, Batra and Love (2005b) found that this criterion fails because it is satisfied at a material point at time t_1 but not at a subsequent time $t_2 > t_1$. Furthermore, the criterion may be satisfied simultaneously at numerous disconnected points but eventually some or all of them do not lie within the region of localization of the deformation. By examining the evolution of different measures of deformation, Batra and Love (2005b) proposed the following criterion for ASB initiation. An ASB initiates at a material point when the rate of energy dissipation there suddenly increases by an order of magnitude.

3.4. Results for WHA with 50% W

Thermo-mechanical deformations of the $2\text{ mm} \times 2\text{ mm}$ quarter specimen, shown in Fig. 1, were analyzed. It enabled us to represent well circular boundaries of W particulates with a 100×100 uniform FE mesh. Two microstructures were considered. The first microstructure was computer generated by distributing randomly $50\text{ }\mu\text{m}$ diameter W particulates, and the volume fraction of W equaled 50%. The second microstructure analyzed was taken from Wei et al.'s (2001) paper; it has different size W particulates, and 90% W by volume. We discuss below results for the first microstructure, and in Section 3.5 those for the second microstructure.

Fig. 2a depicts at $t = 90\text{ }\mu\text{s}$, fringe plots of the effective plastic strain in a $2\text{ mm} \times 2\text{ mm}$ sample meshed with 60×60 uniform 4-node, quadrilateral elements, 20×20 super-elements or patches, and deformed in plane strain tension at a nominal strain rate of 5000/s. Thus, each super element is divided into 3×3 uniform elements. It is clear that the deformation has localized in three regions that cut across boundaries of super-elements as well as finite elements. Whereas inhomogeneities across super-elements boundaries trigger the initiation of an ASB, and probably determine the ASB initiation time, the exact

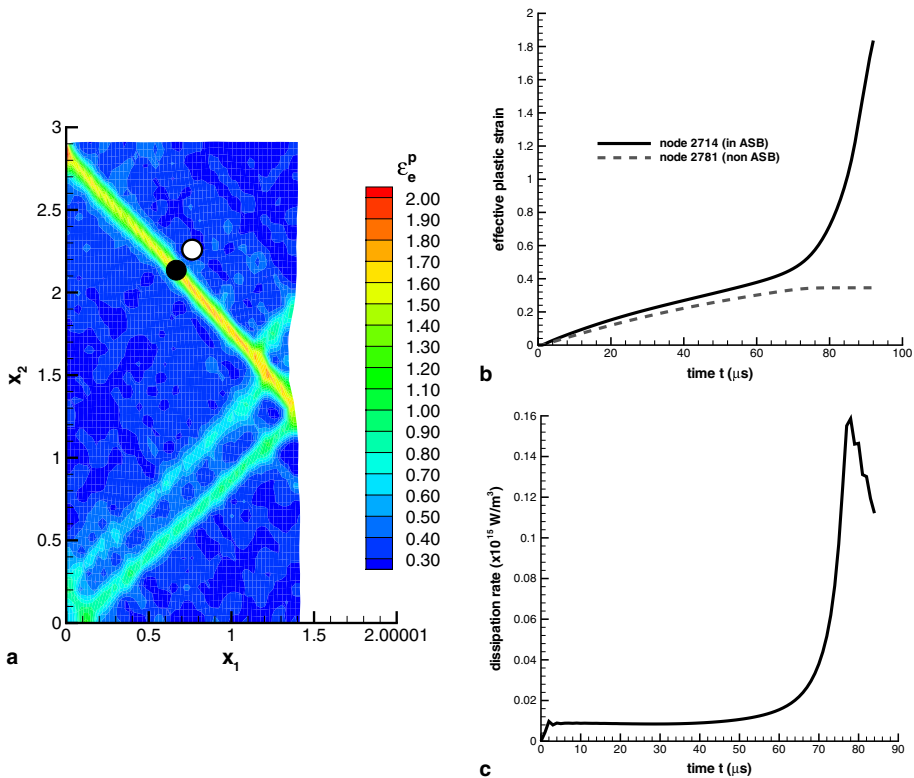


Fig. 2. (a) Fringe plots, at $t = 90\text{ }\mu\text{s}$, of the effective plastic strain in a $2\text{ mm} \times 2\text{ mm}$ sample meshed with 20×20 patches and each patch divided into 3×3 uniform elements and a point (shown with a filled circle) within an ASB and a neighboring point (depicted with an open circle) outside of an ASB. (b) The effective plastic strain versus time for those two points. (c) Energy dissipation rate versus time at a material point within an ASB.

correlation among the ASB initiation time, location, and the number, magnitude and locations of inhomogeneities (or defects) is unknown. [Batra and Wilson \(1998\)](#) analyzed plane strain, and axisymmetric tensile deformations of a 5 mm × 10 mm WHA specimen meshed with 100 × 100 uniform rectangular elements. They assumed that of the 10⁴ elements, a few randomly located elements were comprised of NiFe and the remaining of W. In one of the simulations, an ASB did not pass through either one of the two NiFe elements.

Two points, one within and the other outside the region of localized deformation, are marked in [Fig. 2a](#). From the time histories of the effective plastic strain at these two points exhibited in [2b](#), one can see that at $t \approx 64 \mu\text{s}$ the effective plastic strain begins to increase exponentially at the point within the ASB, but its rate of growth steadily decreases at the point that is outside of the ASB, and becomes essentially zero (i.e., the effective plastic strain approaches a constant value). It implies that subsequent deformation of the material point outside of the ASB are elastic. In [Fig. 2c](#), we have plotted the energy dissipation rate vs. time at the material point located within an ASB. It is clear that the radius of curvature of this curve suddenly decreases at $t \approx 64 \mu\text{s}$ signifying the initiation of the localization of deformation there. Such plots at numerous points, and for different arrangements of particulates, confirmed that the ASB initiation criterion based on the explosive increase in the energy dissipation rate works satisfactorily.

[Batra and Chen \(2001\)](#) have computed the energy dissipation rate within an ASB formed in a thermoviscoplastic material deformed in simple shear. Their values of the energy dissipation rate also showed a peak like that in [Fig. 2c](#), and the peak value occurred when $\tau/\tau_{\text{max}} = 0.62$ for the Johnson–Cook relation. Here τ is the shear stress, and τ_{max} its maximum value at a point during the deformation process. The peak value of the energy dissipation rate and the corresponding value of τ/τ_{max} varied with the thermo-visco-plastic relation even if it had been calibrated against the same test data for homogeneous simple shearing deformations.

We list in [Table 2](#) below the ASB initiation times and the location in the reference configuration of the point from where an ASB initiates for the different analyses. Whereas for the 30 × 30 patchwork analysis, the ASB initiation time is very close to that obtained with the mesoscale analysis, the ASB originates from different points in the two cases.

We note that in a homogenized body with material properties obtained by the rule of mixtures and without introducing a defect, an ASB formed at $t \approx 126 \mu\text{s}$. Deformations become inhomogeneous because of the interaction between incident waves and waves reflected from the boundaries. Truncation errors also introduce small inhomogeneities and may provide nucleation sites for the localization of deformations. [Batra and Love \(2005b\)](#) have found the defect size introduced at the specimen centroid that will give ASB initiation time close to the value obtained with the mesoscale analysis.

For a fixed volume fraction of W, [Batra and Love \(2005b\)](#) have shown that the ASB initiation time varies with the particulate arrangement. For a given volume fraction and

Table 2
ASB initiation times and the location of its point of initiation for different analyses

| # patchwork elements | ASB init. time (μs) | Origination point (ref. config.) |
|-------------------------|----------------------------------|----------------------------------|
| 10 per edge (100 total) | 64.1 | (0.100, 0.000) |
| 20 per edge (400 total) | 63.1 | (1.300, 0.867) |
| 30 per edge (900 total) | 62.3 | (1.767, 1.033) |
| Mesoscale analysis | 61.1 | (1.470, 1.130) |

arrangement of W particulates, the ASB initiation time depends upon the mode of deformation; it is highest for axisymmetric deformations.

3.4.1. Variation of effective plastic strain across an ASB

Fig. 3a shows contour plots of the effective plastic strain, and a straight line perpendicular to an ASB; it is a reproduction of Fig. 2a with an added straight line perpendicular to an ASB. We have exhibited in Fig. 3b and c the variation of the effective plastic strain and the energy dissipation rate with the distance from a fixed point on this line. It is evident that the peak effective plastic strain within the ASB is an order of magnitude larger than that at points outside of the ASB, and the energy dissipation rate is essentially zero at points outside of an ASB. The width of the ASB is about 0.15 mm which is probably an order of magnitude larger than the observed value. Previous analyses of similar problems have indicated that the band width is mesh-dependent but a reasonably fine mesh such as the one employed here predicts correctly the qualitative features of the localization of deformation, and the ASB initiation time.

The primary objective of this work is to delineate the effect of the number of patches or super-elements. Results included in Table 2 indicate that 30×30 patches are sufficient to

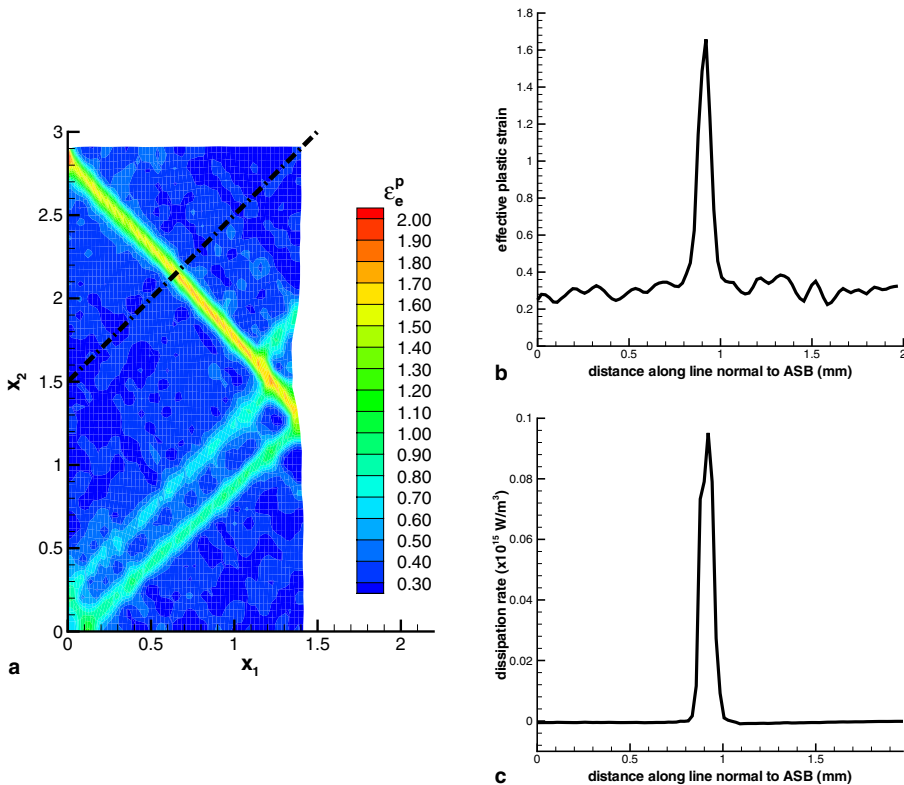


Fig. 3. (a) A contour plot, at $t = 90 \mu\text{s}$, of the effective plastic strain for a $2 \text{ mm} \times 2 \text{ mm}$ sample meshed with 60×60 elements and 20×20 patches. The dotted line perpendicular to an ASB is used in (b). (b,c) A plot of the effective plastic strain and the energy dissipation rate versus distance along the dotted line in (a).

get ASB initiation time with 2% accuracy for a WHA with 50% volume fraction of 55 μm diameter randomly distributed W particulates.

3.5. Results for WHA with 90% W

Plane strain tensile deformations of a 10 mm \times 10 mm sample of actual microstructure, depicted in Fig. 4a, and taken from Wei et al.’s (2001) paper were analyzed. The given microstructure is for a region much smaller than the size of the sample used in the analysis.

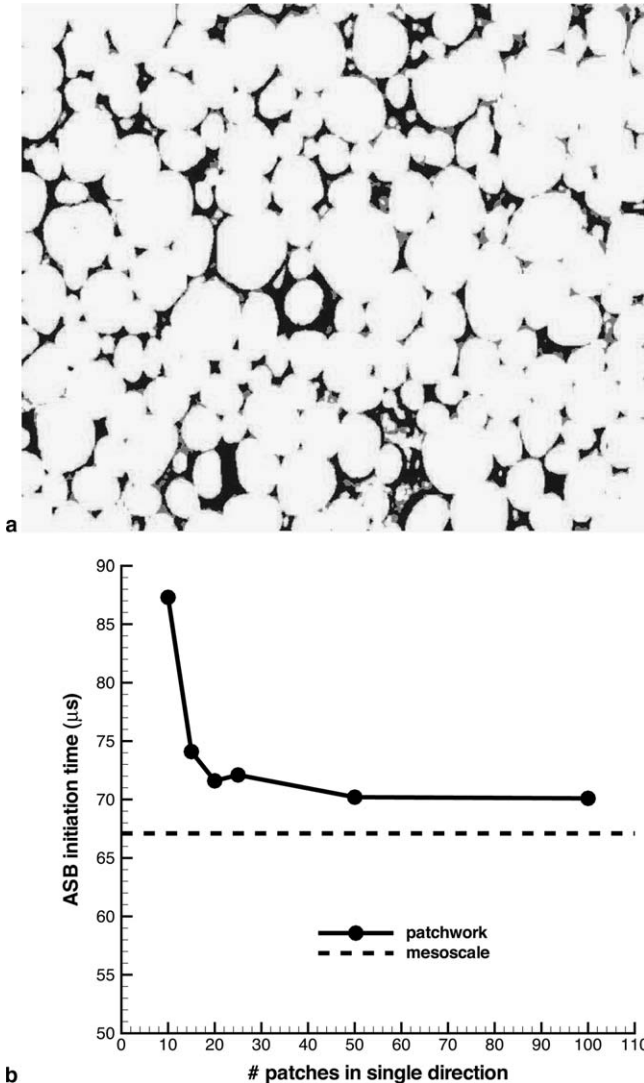


Fig. 4. (a) Actual microstructure of tungsten heavy alloy with 90% volume fraction of tungsten; Wei et al. (2001). White regions are occupied by tungsten, and dark by NiFe. (b) ASB initiation time versus patch size for a 10 mm \times 10 mm sample (a quarter was meshed with 100 \times 100 elements) for an actual microstructure of a WHA.

The microstructure in the specimen was assumed to be symmetrical about the horizontal and the vertical centroidal axes so that deformations of only a quarter of the specimen deformed at a nominal strain rate of 5000/s could be analyzed. The $5\text{ mm} \times 5\text{ mm}$ region was divided into a uniform FE mesh of 100×100 elements. The solution so computed is compared with those obtained by dividing the $5\text{ mm} \times 5\text{ mm}$ region into super-elements of different sizes but with 100×100 uniform elements in the $5\text{ mm} \times 5\text{ mm}$ region.

The plot in Fig. 4b of the ASB initiation time vs. the number of uniform super-elements in either the X_1 - or the X_2 -direction shows that the ASB initiation time converges with an increase in the number of super-elements. The converged value, $70\text{ }\mu\text{s}$, of the ASB initiation time differs from the ASB initiation time of $67\text{ }\mu\text{s}$ computed with the meso-scale analysis by less than 5%. Whereas the meso-scale analysis required nearly 120 h of CPU time on a SGI Altix machine the patchwork analysis needed only 5 h of CPU time. We note that the difference in the ASB initiation times with the 50×50 and the 100×100 patches is indeed very small. Thus one can analyze several different microstructures with the patchwork, and then study the final one or two with the meso-scale analysis. The computed ASB initiation time could not be compared with that found by Wei et al. (2001) since they tested specimens in torsion, and we have simulated plane strain tensile deformations.

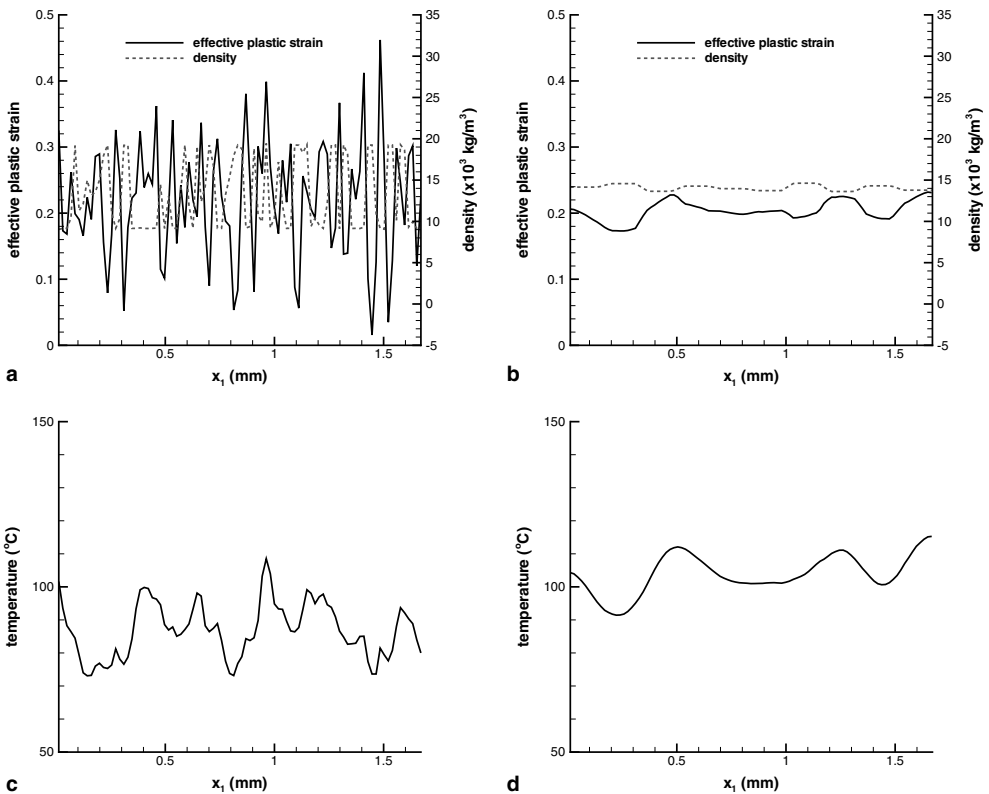


Fig. 5. At $t = 40\text{ }\mu\text{s}$, variation on the line $x_2 = 1.5\text{ mm}$ of the effective plastic strain and the temperature obtained with (a,c) the meso-scale, and (b,d) the patchwork analysis.

Furthermore, Wei et al. (2001) neither report the ASB initiation criterion nor the ASB initiation time.

Whereas the patchwork technique gives very good values of the ASB initiation times the deformation fields within the specimen differ noticeably from those computed with the meso-scale analysis. For example, we have plotted in Fig. 5a and b the distribution on the line $x_2 = 1.5$ mm of the effective plastic strain at $t = 40 \mu\text{s}$ computed both with the mesoscale and the patchwork analyses. The distribution of the mass density is also shown to identify whether a material particle is made of W (high density) or NiFe (low density). It is clear that the meso-scale analysis gives sharp gradients in the effective plastic strain in regions adjoining the interfaces between two different particulates. The effective plastic strain is usually much larger in NiFe than that in W. As expected, the patchwork analysis smears out these sharp gradients in the mass density and the effective plastic strain.

Fig. 6a and b shows results similar to those of Fig. 5a and b at time $t = 80 \mu\text{s}$ which exceeds the ASB initiation time. In the post-localization regime, the mesoscale and the patchwork analyses give quite different spatial gradients of the effective plastic strain. Note that at either one of these two times the spatial variation of the effective plastic strain for the patchwork analysis cannot be obtained by averaging values at two successive locations computed with the mesoscale analysis.

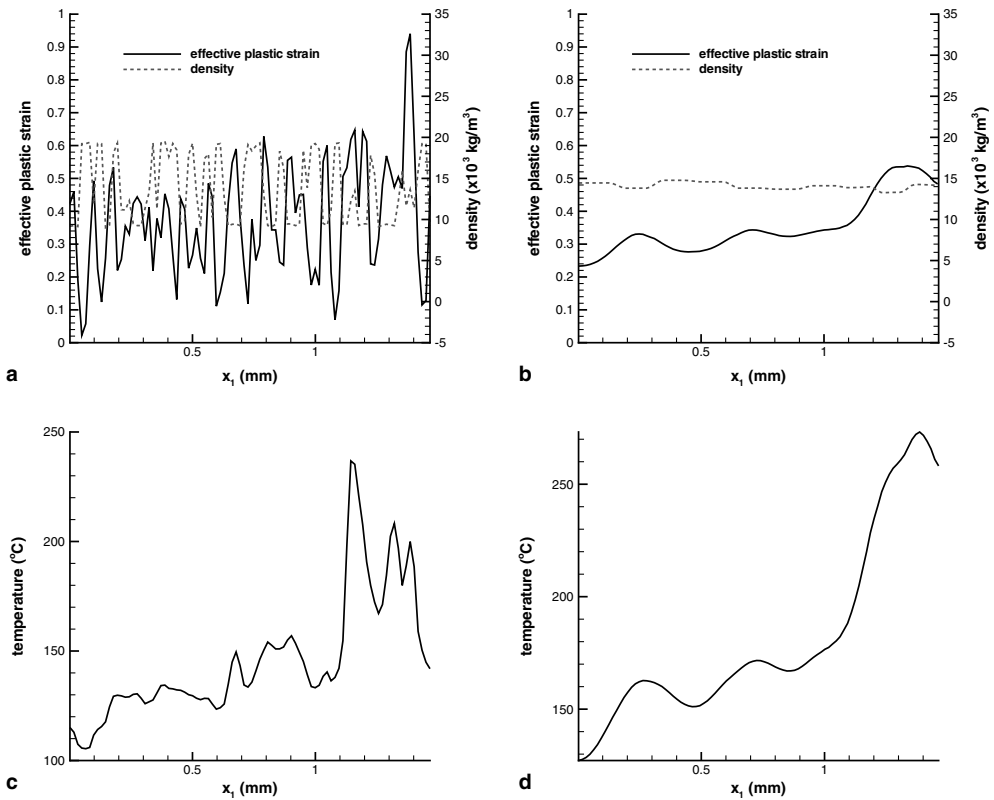


Fig. 6. At $t = 80 \mu\text{s}$, variation on the line $x_2 = 1.5$ mm of the effective plastic strain and the temperature obtained with (a,c) the meso-scale, and (b,d) the patchwork analysis.

4. Conclusions

We have analyzed the initiation and the development of adiabatic shear bands in a particulate composite comprised of tungsten particulates immersed in nickel–iron matrix, and deformed in plane strain tension at a nominal strain rate of 5000/s. Particulates are assumed to be perfectly bonded to the matrix and the two are in perfect thermal contact. Effects of heat conduction, thermal expansion, thermal softening, strain- and strain-rate hardening, and the degradation of material moduli with the evolution of porosity are incorporated in the analysis of the problem. The problem is analyzed first by considering material properties of the particulates and the matrix, and then by dividing it into a number of uniform patches with material properties in each patch obtained by a homogenization technique. For the latter analysis, the cross-section is divided into a number of same-size inhomogeneous bodies. It is found that with an increase in the number of patches, the adiabatic shear band initiation time converges to that obtained with the meso-scale analysis. However, the material point from where an adiabatic shear band initiates is different in the two cases. Furthermore, the gradients in the effective plastic strain for the meso-scale analysis are much higher than those in the patch-work analysis. Thus, if one is interested in only the adiabatic shear band initiation time then the patch work analysis provides very good results with a considerable saving in computational resources. However, one needs to perform the mesoscale analysis to capture finer details of deformation fields. A possibility is to examine several initial microstructures with the patchwork analysis, and the final few with the high fidelity mesoscale analysis.

Acknowledgements

This work was partially supported by the NSF Grant CMS0002849, the ONR Grants N00014-98-1-0300 and N00014-03-MP-2-0131, the ARO Grant DAAD19-01-1-0657, a subcontract from the Kennametal Inc., and the AFOSR MURI to Georgia Institute of Technology with a subcontract to Virginia Polytechnic Institute and State University. Views expressed in the paper are those of authors and not of funding agencies.

References

- Bai, Y., Dodd, B., 1992. *Adiabatic Shear Localization-Occurrence, Theories and Applications*. Pergamon Press, New York.
- Batra, R.C., 1975. On heat conduction and wave propagation in non-simple rigid solids. *Lett. Appl. Eng. Sci.* 3, 97–107.
- Batra, R.C., 1980. Finite plane strain deformations of rubberlike materials. *Int. J. Numer. Meth. Eng.* 15, 145–160.
- Batra, R.C., 1987. The initiation and growth of, and the interaction among adiabatic shear bands in simple and dipolar materials. *Int. J. Plast.* 3, 75–89.
- Batra, R.C., 1988. Steady state penetration of thermoviscoplastic targets. *Comput. Mech.* 3, 1–12.
- Batra, R.C., Chen, L., 1999. Shear band spacing in gradient-dependent thermoviscoplastic materials. *Comput. Mech.* 23, 8–19.
- Batra, R.C., Chen, L., 2001. Effect of viscoplastic relations on the instability strain, shear band initiation strain, the strain corresponding to the minimum shear band spacing, and the band width in a thermoviscoplastic material. *Int. J. Plast.* 17, 1465–1489.
- Batra, R.C., Jaber, N.A., 2001. Failure mode transition speeds in an impact loaded prenotched plate with four thermoviscoplastic relations. *Int. J. Fracture* 110, 47–71.

- Batra, R.C., Jin, X.S., 1994. Analysis of dynamic shear bands in porous thermally softening viscoplastic materials. *Arch. Mech.* 46, 13–36.
- Batra, R.C., Kim, C.H., 1990a. Adiabatic shear banding in elastic-viscoplastic nonpolar and dipolar materials. *Int. J. Plast.* 6, 127–141.
- Batra, R.C., Kim, K.H., 1990b. Effect of viscoplastic flow rules on the initiation and growth of shear bands at high strain rates. *J. Mech. Phys. Solids* 38, 859–874.
- Batra, R.C., Kim, C.H., 1991. Effect of thermal conductivity on the initiation and growth of adiabatic shear bands in steels. *Int. J. Eng. Sci.* 29, 949–960.
- Batra, R.C., Kim, C.H., 1992. Analysis of shear banding in twelve materials. *Int. J. Plast.* 8, 425–452.
- Batra, R.C., Ko, K.I., 1992. An adaptive mesh refinement technique for the analysis of shear bands in plane strain compression of a thermoviscoplastic solid. *Comput. Mech.* 10, 369–379.
- Batra, R.C., Ko, K.I., 1993. Analysis of shear bands in dynamic axisymmetric compression of a thermoviscoplastic cylinder. *Int. J. Eng. Sci.* 31, 529–547.
- Batra, R.C., Lear, M.H., 2005. Adiabatic shear banding in plane strain tensile deformations of 11 thermoviscoplastic materials with finite wave speed. *Int. J. Plast.* 21, 1521–1545.
- Batra, R.C., Liang, X.Q., 1997. Finite deformations of smart structures. *Comp. Mech.* 20, 427–438.
- Batra, R.C., Liu, D.-S., 1989. Adiabatic shear banding in plane strain problems. *J. Appl. Mech.* 56, 527–534.
- Batra, R.C., Love, B.M., 2004. Adiabatic shear bands in functionally graded materials. *J. Thermal Stress.* 27, 1101–1123.
- Batra, R.C., Love, B.M., 2005a. Crack propagation due to brittle and ductile failures in microporous thermoelastoviscoplastic functionally graded materials. *Eng. Fracture Mech.* 72, 1954–1979.
- Batra, R.C., Love, B.M., 2005b. Mesoscale analysis of shear bands in high strain rate deformations of tungsten/nickel-iron composites. *J. Thermal Stress.* 28, 747–782.
- Batra, R.C., Love, B.M., 2006a. Multiscale analysis of adiabatic shear bands in tungsten heavy alloy particulate composites. *Int. J. Multiscale Comput. Eng.*, in press.
- Batra, R.C., Love, B.M., 2006b. Determination of effective thermomechanical parameters of a mixture of two thermoviscoplastic constituents. *Int. J. Plast.* 22, 1026–1061.
- Batra, R.C., Wei, Z.G., 2006. Shear bands due to heat flux prescribed at boundaries. *Int. J. Plast.* 22, 1–15.
- Batra, R.C., Wilson, N.M., 1998. Adiabatic shear bands in plane strain deformations of a WHA. *Int. J. Plast.* 14, 43–60.
- Bodner, S.R., Partom, Y., 1975. Constitutive equations for elastic-viscoplastic strain-hardening materials. *J. Appl. Mech.* 56, 385–389.
- Budiansky, B., 1990. Thermal and thermoelastic properties of isotropic composites. *J. Compos. Mater.* 4, 701–744.
- Cattaneo, C.A., 1958. A form of heat equation which eliminates the paradox of instantaneous propagation. *CR Acad. Sci.* 247, 431–433.
- Charalambakis, N., Baxevanis, T., 2004. Adiabatic shearing of non-homogeneous thermoviscoplastic materials. *Int. J. Plast.* 20, 899–914.
- Chatzigeorgiou, G., Charalambakis, N., 2005. Instability analysis of non-homogeneous materials under biaxial loading. *Int. J. Plast.* 21, 1970–1999.
- Chiu, T.C., Erdogan, F., 1999. One-dimensional wave propagation in a functionally graded medium. *J. Sound Vib.* 222, 453–487.
- Chu, C., Needleman, A., 1980. Void nucleation effects in biaxially stretched sheets. *J. Eng. Mater. Technol.* 102, 249–256.
- Dai, L.H., Liu, L.F., Bai, Y.L., 2004. Formation of adiabatic shear bands in metal matrix composites. *Int. J. Solids Struct.* 41, 5979–5993.
- Dick, R.D., Ramachandran, V., Williams, J.D., Armstrong, R.W., Holt, W.H., Mock Jr., W., 1991. Dynamic deformation of W7Ni3Fe alloy via reverse-ballistic impact. In: Crowson, A., Chen, E.S. (Eds.), *Tungsten and Tungsten Alloys-Recent Advances*. The Minerals, Metals & Materials Society, pp. 269–276.
- Gurson, A.L., 1977. Continuum theory of ductile rupture by void nucleation and growth: Part I. *J. Eng. Mater. Technol.* 99, 2–15.
- Hindmarsh, A.C., 1983. ODEPACK – a systematized collection of ODE solvers. In: Stepleman, R.S. et al. (Eds.), *Scientific Computing*. North-Holland, Amsterdam.
- Hughes, T.J.R., 1987. *Finite Element Method*. Prentice-Hall, Englewood Cliffs, NJ.
- Jiang, B., Batra, R.C., 2002. Effective properties of a piezocomposite containing shape memory alloy and inert inclusions. *Continuum Mech. Thermodyn.* 14, 87–111.

- Johnson, G.R., Cook, W.H., 1983. A constitutive model and data for metals subjected to large strains, high strain-rates, and high temperatures. In: Proceedings of the 7th International Symposium on Ballistics, pp. 541–547.
- Needleman, A., 1989. Dynamics shear band development in plane strain. *J. Appl. Mech.* 56, 1–9.
- Mori, T., Tanaka, K., 1973. Average stress in matrix and average elastic energy of materials with misfitting inclusions. *Acta Metall.* 21, 571–574.
- Tresca, H., 1878. On further application of the flow of solids. *Proc. Inst. Mech. Eng.* 30, 301–345.
- Tvergaard, V., Needleman, A., 1984. Analysis of the cup-cone fracture in a round tensile bar. *Acta Metall.* 32, 157–169.
- Vernotte, P., 1958. The true heat equation. *CR Acad. Sci.* 247, 2103.
- Wei, Z.G., Batra, R.C., 2002. Dependence of instability strain upon damage in thermoviscoplastic materials. *Arch. Mech.* 54, 691–707.
- Wei, Z.G., Yu, J., Li, J., Li, Y., Hu, S., 2001. Influence of stress condition on adiabatic shear localization of tungsten heavy alloys. *Int. J. Impact Eng.* 26, 843–852.
- Wright, T.W., 2002. *The Physics and Mathematics of Adiabatic Shear Bands*. Cambridge University Press, Cambridge.
- Zhou, M., 1993. Dynamic shear localization in a tungsten heavy alloy and ductile rupture in a spheroidized 1045 steel. Doctoral dissertation, Brown University, Providence, RI.
- Zhu, Z.G., Batra, R.C., 1990. Dynamic shear band development in plane strain compression of a viscoplastic body containing a rigid inclusion. *Acta Mech.* 84, 89–107.